Applied Catalysis B: Environmental 249 (2019) 246–256

Contents lists available at ScienceDirect

Applied Catalysis B: Environmental

journal homepage: www.elsevier.com/locate/apcatb

Distinctive ternary CdS/Ni_2P/g-C_3N_4 composite for overall water splitting: Ni_2P accelerating separation of photocarriers

Heng He[a], Jing Cao[a], Minna Guo[a], Haili Lin[a,b,*], Jinfeng Zhang[c,d,**], Yong Chen[e], Shifu Chen[a,***]

[a] College of Chemistry and Materials Science, Huaibei Normal University, Huaibei, 235000, Anhui, PR China
[b] State Key Laboratory of Structural Chemistry, Fuzhou, 350002, Fujian, PR China
[c] College of Physics and Electronic Information, Huaibei Normal University, Huaibei, 235000, Anhui, PR China
[d] State Key Laboratory of Advanced Technology for Materials Synthesis and Processing, Wuhan University of Technology, Wuhan, 430070, Hubei, PR China
[e] Key Laboratory of Photochemical Conversion and Optoelectronic Materials, Technical Institute of Physics and Chemistry, Chinese Academy of Sciences, Beijing, 100190, PR China

ARTICLE INFO

Keywords:
Overall water splitting
Transition metal phosphides
Electron-bridge

ABSTRACT

Efficient overall water splitting over semiconductor photocatalyst is vital but difficult for resolving the energy and environmental crises. In this report, a novel transition metal phosphide Ni_2P-based ternary CdS/Ni_2P/g-C_3N_4 composite was constructed for achieving efficient overall water splitting activity under visible light ($\lambda > 420$ nm). The H_2 and O_2 evolution ratios are 15.56 and 7.75 $\mu mol \cdot g^{-1} h^{-1}$ over CdS/Ni_2P/g-C_3N_4 with 3 wt % Ni_2P, respectively, which is 4.02 times higher than that of binary type II CdS/g-C_3N_4. The separation efficiency of photocarriers of CdS/Ni_2P/g-C_3N_4 is enhanced through greatly speeding up the transfer efficiency of electrons from the conduction band of g-C_3N_4 to that of CdS using Ni_2P as electron-bridge, proved by the photoluminescence, transient photocurrent measurements and electrochemical impendence spectroscopy. The significant finding of this paper sheds light on the important role of transition metal phosphide as electron-bridge to connect the two conduction bands of type II semiconductor heterojuction for strengthening the separation efficiency of photocarriers.

1. Introduction

Solar overall water splitting for H_2 and O_2 evolution is a fascinating and potential strategy for resolving the energy and environmental crises [1–4]. However, it is not easy to satisfy the potential standards for H_2 and O_2 generation simultaneously for a pure substance. Traditional electrochemistry method can successfully produce H_2 and O_2 [5,6], however, large amount of energy also be consumed at the same time. Therefore, solar overall water splitting on the basis of semiconductor photocatalysis technology is very attractive. Nevertheless, only a few photocatalysts are considered as potential research objects, thereinto, CdS and graphite-like carbon nitride (g-C_3N_4) are the representatives used for the overall water splitting under visible light [7,8]. It should be noted that, the biggest difficulty is still the fast recombination rate of photocarriers, which hinders the enhancement of photocatalytic activity.

As for the pure CdS and g-C_3N_4 photocatalysts, their photocarriers have low separation efficiency if only relying on the intrinsic inner electric field [9,10]. Thus, novel CdS/g-C_3N_4 heterojunction with typical type II energy band structure was designed on account of the interfacial effect for photocarriers separation [11,12]. It is well known that the interface resistance always exists during the photocarriers transfer process under light irradiation, which reduces the separation efficiency of photocarriers remarkably. As is reported, noble metals (Au, Ag, Pt) [13–15] with high electrical conductivity are commonly used as “electron-bridge” in an indirect Z-scheme composite system to lead the transfer of electrons from one component to combine with the holes on another component quickly, which reduces the interface resistance vastly between the two components. So, it is very potential to construct an efficient electron-bridge between the conduction bands of CdS/g-C_3N_4 composite.

Generally speaking, traditional excellent electron-bridge (Au, Ag, Pt) has the basic characteristics of high electrical conductivity. Because noble metals are high expensive, some alternatives including non-noble metals (Cu [16], W [17] and Cd [18]), reduced graphene oxide (RGO) [19–21], C quantum dots [22,23], even surface oxygen defects [24,25]

* Corresponding author at: College of Chemistry and Materials Science, Huaibei Normal University, Huaibei, 235000, Anhui, PR China.
** Corresponding author at: College of Physics and Electronic Information, Huaibei Normal University, Huaibei, 235000, Anhui, PR China.
*** Corresponding author.
E-mail addresses: linhaili@mail.ipc.ac.cn (H. Lin), zjf_y2004@126.com (J. Zhang), chshifu@chnu.edu.cn (S. Chen).

https://doi.org/10.1016/j.apcatb.2019.02.055
Received 11 November 2018; Received in revised form 1 February 2019; Accepted 20 February 2019
Available online 28 February 2019
0926-3373/

have been developed as electron mediators to improve the separation of photocarriers. As is known to all, transition metal phosphides (TMPs) praised as quasi-platinum catalyst [26] can capture electrons intensively. In this case, TMPs can be applied as one of the potential electron-bridges because they are not only good conductors of electricity and heat, but also they are composed of earth-abundant elements and are inexpensive [27]. Therefore, TMPs have wide industrial applications, such as hydrodesulfurization [28], hydrodenitrogenation [29], electrocatalytic reaction [30] and photocatalytic reaction [31]. TMPs also have extensive potentials in magnetic, photonic, electronic and data storage devices due to their novel magnetic and semiconducting properties [32]. Considering the excellent electrical conductivity, TMPs have great advantages for applying as novel, low price and highly efficient electron-bridge in CdS/g-C_3N_4 heterojunction system. However, to the best of our knowledge, there are no reports on the application of TMPs as electron-bridge in an overall water splitting system.

In this paper, a distinctive ternary CdS/Ni_2P/g-C_3N_4 composite was constructed, in which the Ni_2P was stuck in the middle of CdS and g-C_3N_4. Under visible light ($\lambda > 420$ nm), CdS/Ni_2P/g-C_3N_4 shows outstanding overall water splitting activity for H_2 and O_2 evolution compared to CdS/g-C_3N_4. The existence of Ni_2P greatly reduced the recombination of photocarriers, proved by the photoluminescence, transient photocurrent measurements and electrochemical impendence spectroscopy. The significant finding of this paper opens a new window for TMPs as novel electron-bridge in type II heterojunction system for overall water splitting application.

2. Experimental

2.1. Preparation of CdS/Ni_2P/g-C_3N_4

All chemicals with analytical purity were obtained from Sinopharm Chemical Reagent Co., Ltd. and were used without further purification. Deionized water was employed in all experiments.

Ternary CdS/Ni_2P/g-C_3N_4 composite was prepared according to the following 3 steps, as shown in Fig. 1.

Firstly, g-C_3N_4 was prepared on the basis of the previous work [33]. That is, the g-C_3N_4 substrate was prepared by directly heating melamine at 550 °C in a crucible with a cover in air for 4 h with a heating rate of 5.0 °C/min. After cooling to the room temperature, the temperature was raised to 550 °C again with a heating rate of 5.0 °C/min and kept for 2 h. After cooling to the room temperature again, the g-C_3N_4 was obtained.

Secondly, the Ni_2P/g-C_3N_4 was synthesized by a hydrothermal method [34]. In a typical process, 0.50 *g* g-C_3N_4 powder was dispersed in 40.0 mL deionized water homogeneously and then 0.101 mmol Ni$(NO_3)_2 \cdot 6H_2O$ was dissolved in the above dispersion completely. Subsequently, 1.013 mmol red P was further dispersed in above-mentioned dispersion. After the dispersion was transferred to a 50 mL Teflon stainless steel autoclave, it was sealed and maintained at 140 °C for 10 h. Finally, the product was centrifuged, rinsed with water and ethanol, respectively, dried at 70 °C for 10 h. As comparison, Ni_2P/CdS was also synthesized under the identical synthetic condition of Ni_2P/g-C_3N_4 in the presence of CdS. Pure Ni_2P was also prepared as reference using the same method in the absence of g-C_3N_4 or CdS.

Thirdly, the CdS/Ni_2P/g-C_3N_4 was fabricated by a solvothermal method. In detail, 0.50 *g* Ni_2P/g-C_3N_4 powder and 0.545 mmol Cd$(NO_3)_2 \cdot 4H_2O$ were added into 40 mL ethylenediamine and stirred for 12 h at room temperature. Subsequently, 0.545 mmol $CS(NH_2)_2$ was dissolved in the mixture and then the dispersion was transferred to a 50 mL Teflon stainless steel autoclave. After keeping the temperature at 160 °C for 12 h, the product was centrifuged, rinsed with water and ethanol, respectively, dried at 70 °C for 10 h. The theoretical content of Ni_2P in the CdS/Ni_2P/g-C_3N_4 composite was 1.3 wt%.

As reference, pure CdS and CdS/g-C_3N_4 composite were also prepared using the same method, respectively.

2.2. Characterization

The crystal phases of the samples were investigated using a BRUKER D8 ADVANCE X-ray diffractometer (XRD) with a scanning speed of 10°/min and Cu Kα radiation ($\lambda = 1.5406$ Å). The morphologies of the as-prepared samples were examined by a FEI Sirion 200 field emission scanning electron microscope (FESEM) with 5.00 kV scanning voltages. TEM and HRTEM images and selected area energy dispersive X-ray (EDX) spectra were obtained on a JEOL-2011 transmission electron microscope coupled with an EDX detector (Oxford) with an accelerating voltage of 200 kV. XPS data were gained by a Thermo ESCALAB 250 with Al Kα (1486.6 eV) line at 150 W. BET specific surface area of the powder was determined by a Micromeritics ASAP2020 apparatus at liquid nitrogen temperature (77.3 K). The optical absorption properties of the samples were analyzed with a TU-1901 UV–vis spectrophotometer in the range of 300–800 nm wavelengths. The photoluminescence (PL) spectra were measured on a JASCO FP-8300 spectrofluorometer with 370 nm excitation wavelength.

2.3. Photoelectrochemical measurements

Transient photocurrent experiments were conducted on an

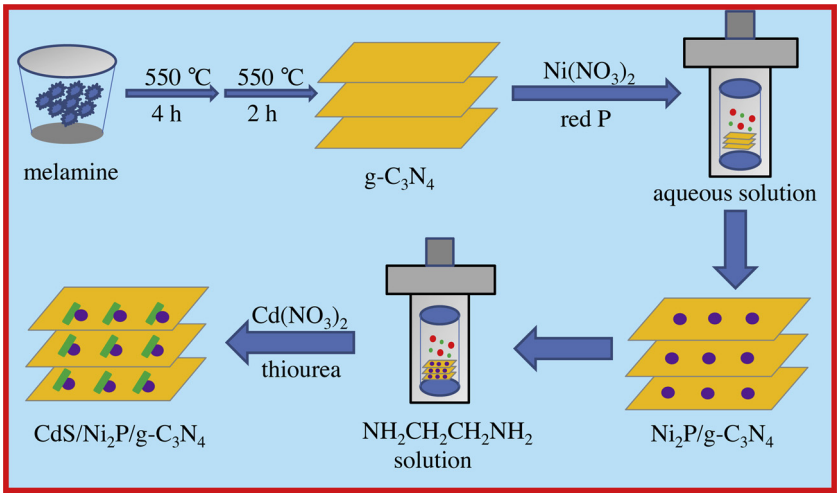

Fig. 1. Schematic diagram of the synthetic route of ternary CdS/Ni_2P/g-C_3N_4 composite.

electrochemical analyzer (CHI660E, Chenhua Instruments Co. Shanghai, China) with a working electrode, a Pt counter electrode and an Ag/AgCl (3.0 M KCl) reference electrode. A 300 W Xe lamp with a 420 nm UV cut-off filter was used as the light source. The electrolyte was phosphate buffered saline consisting of 0.1 M Na_2HPO_4 and 0.1 M NaH_2PO_4 aqueous solution. The preparation process of working electrode was similar to our recent report [35]. Typically, 50 mg of sample was mixed with 1.0 mL of chitosan firstly, and then kept sonication for 20 min to get the homogeneous slurry. The slurry was coated onto the conductive surface of ITO glass and all the solid films should possess the similar size and thickness. Subsequently, the as-obtained sample films were dried at 80 °C for 2 h in air to acquire working electrodes. The Mott-Schottky plots were evaluated under the same conditions as the transient photocurrent experiments except without the Xe lamp irradiation. Electrochemical impedance spectroscopy (EIS) measurements using the above-mentioned working electrodes were also carried out under the condition of visible light illumination, a perturbation of 5 mV was applied to the electrodes over a frequency range of 0.01-10^4 Hz and 0.2 M KCl solution was used as the electrolyte.

2.4. Photocatalytic activity investigation

Photocatalytic overall water splitting was evaluated on a photocatalytic system (CEL-SPH2N, Beijing China Education Au-light Co., Ltd.). In a typical photocatalytic experiment, 50 mg of photocatalyst was dispersed in a 50 mL of ultrapure water without any sacrificial agent. Then, the reaction system was vacuumized for 30 min meanwhile the reactor temperature was cooled to 6 °C by a circular cooling water system. Afterwards, the reactor was irradiated by a 300 W Xe lamp with a 420 nm cut-off filter for 2 h. The generated H_2 and O_2 were analyzed by a gas chromatograph (GC-9790II, TCD detector with Ar as carrier gas) equipped with a 5 Å molecular sieve column.

3. Results and discussion

3.1. Characterization

3.1.1. XRD analysis

Fig. 2a shows the XRD patterns of the as-prepared samples. It is found that pure g-C_3N_4 has obvious diffraction peaks at 13.0° and 27.7°, which correspond to the (100) and (002) planes of g-C_3N_4 with the hexagonal phase structure (JCPDS file No. 87-1526) [36], respectively. Pure CdS also has strong diffraction peaks located at 25.0°, 26.8°, 28.4°, 43.8°, 48.1° and 52.0°, corresponding to the (100), (002), (101), (110), (103) and (112) planes of CdS with the hexagonal phase structure (JCPDS file No. 65-3414), respectively, implying CdS has good crystallinity. Besides, the XRD patterns of Ni_2P sample matches well with the hexagonal phase standard card of Ni_2P (JCPDS file No. 65-3544) with (111), (201), (210) and (002) planes, respectively. The binary Ni_2P/g-C_3N_4 composite only shows the diffraction peaks of g-C_3N_4 due to the low amount of Ni_2P [37,38], this phenomenon is also observed for Ni_2P/CdS sample. However, even though g-C_3N_4 occupies high contents in CdS/g-C_3N_4 and CdS/Ni_2P/g-C_3N_4 samples, the peak intensity of (002) still appears very low because of the excellent crystallinity of CdS, as is depicted in the enlarged XRD patterns in Fig. 2b and c. The similar results were also reported in previous studies [11,39].

3.1.2. XPS analysis

To investigate the components, electronic states and their interaction, pure CdS, Ni_2P, g-C_3N_4 and CdS/Ni_2P/g-C_3N_4 composite were measured by XPS technology. As shown in Fig. 3a, CdS contains Cd and S elements, Ni_2P is composed of Ni, P and O elements, and meanwhile g-C_3N_4 includes C and N elements. As for the ternary CdS/Ni_2P/g-C_3N_4 sample, it comprises C, N, O, Ni, P, Cd and S elements. It is necessary to note that, the extra O peaks attribute to the H_2O molecules adhered on the surface of samples and the metal phosphate salts originating from surface oxidation of Ni_2P [40–42].

The high resolution XPS spectra of C, N, Ni, P, Cd and S elements are also provided in Fig. 3b–g. Compared to pure CdS, Ni_2P and g-C_3N_4, the corresponding peaks of ternary CdS/Ni_2P/g-C_3N_4 composite shift

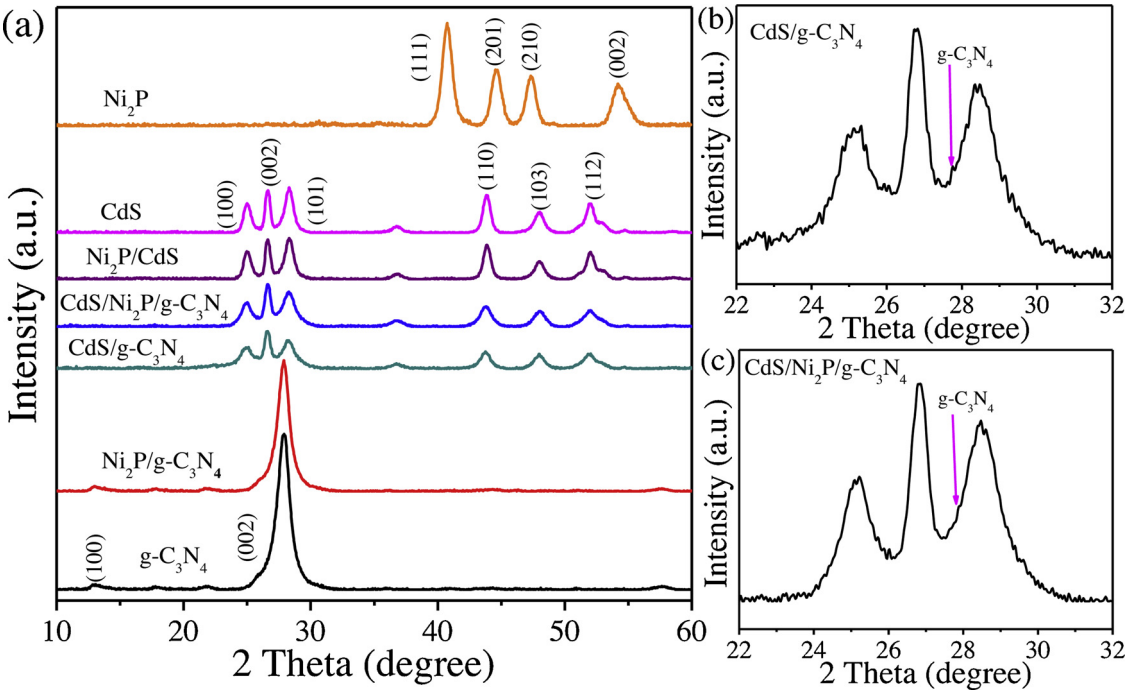

Fig. 2. XRD patterns of CdS/Ni_2P/g-C_3N_4 and corresponding reference samples.

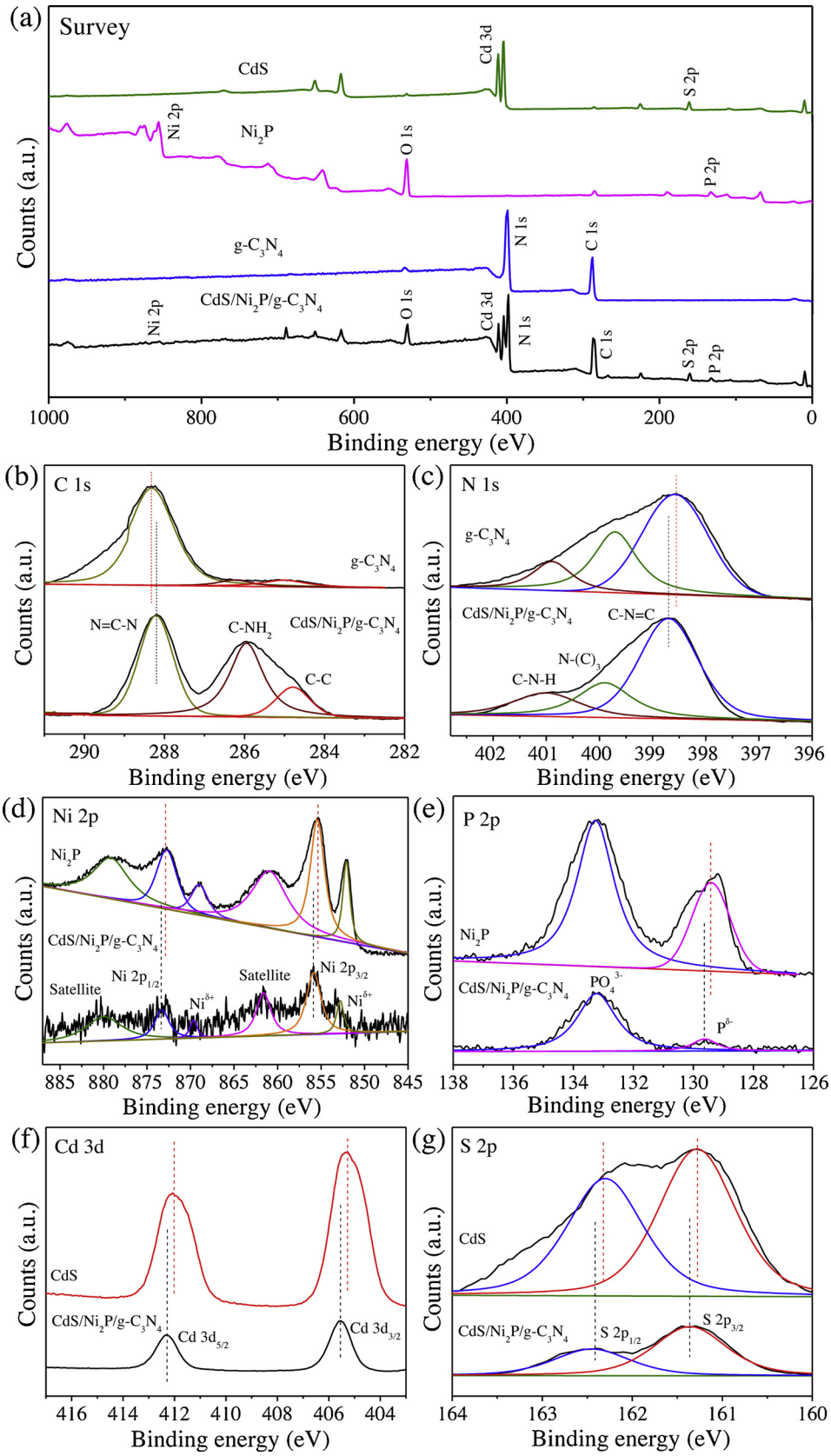

Fig. 3. XPS spectra of CdS, Ni_2P, g-C_3N_4 and CdS/Ni_2P/g-C_3N_4 composite: (a) survey spectra, (b) C 1 s, (c) N 1 s, (d) Ni 2p, (e) P 2p, (f) Cd 3d and (g) S 2p.

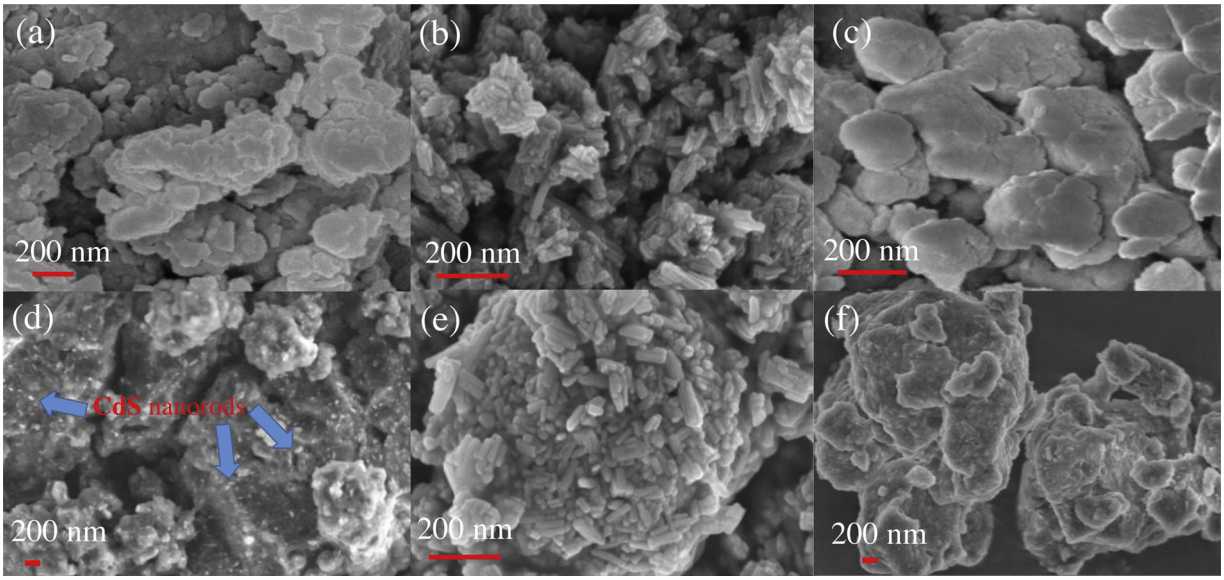

Fig. 4. SEM images of (a) g-C_3N_4, (b) CdS, (c) Ni_2P/g-C_3N_4, (d) CdS/g-C_3N_4, (e) Ni_2P/CdS and (f) CdS/Ni_2P/g-C_3N_4.

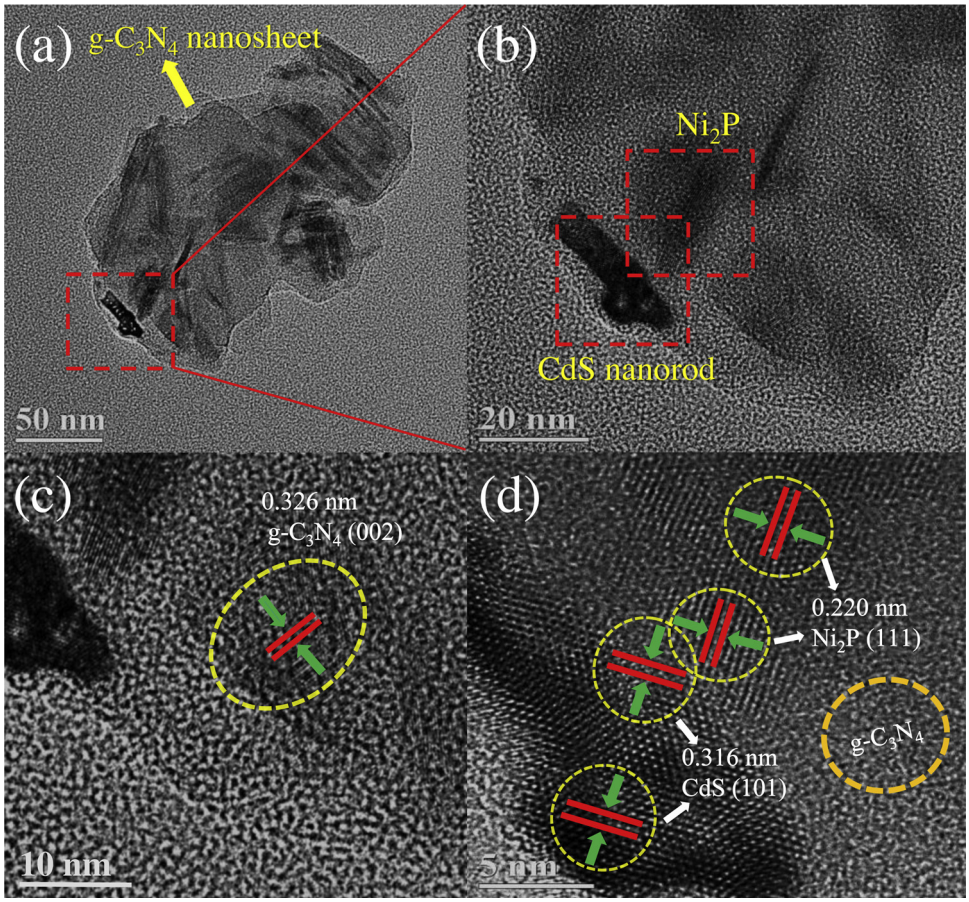

Fig. 5. (a) and (b) TEM images, (c) and (d) HRTEM images of CdS/Ni_2P/g-C_3N_4.

slightly owing to the close interaction among the three components [43,44]. In detail, C 1s has three peaks at binding energies of 288.2, 285.9 and 284.8 eV (Fig. 3b), corresponding to N=C–N, C–NH_2 and C–C species of g–C_3N_4 [45–47], respectively. It is different from pure g-C_3N_4, the peak intensity of C–NH_2 and C–C in CdS/Ni_2P/g-C_3N_4 sample becomes high, indicating the polymerization degree of g-C_3N_4 substrate reduced obviously [33], which mainly stems from the effect of continuously hydrothermal and solvothermal synthesis processes [48]. The N 1 s XPS peak (Fig. 3c) can be divided into three peaks located at 401.0, 400.0 and 398.9 eV, respectively. The main peak at 398.9 eV derives from the sp^2-bonded N that involves in the triazine rings (C–N=C) of g-C_3N_4 [49]. Additionally, the other two peaks at 400.0 and 401.0 eV can be assigned to N-$(C)_3$ and CNH [48,50], respectively.

There are six peaks at 880.5, 873.5, 869.7, 861.8, 855.8 and

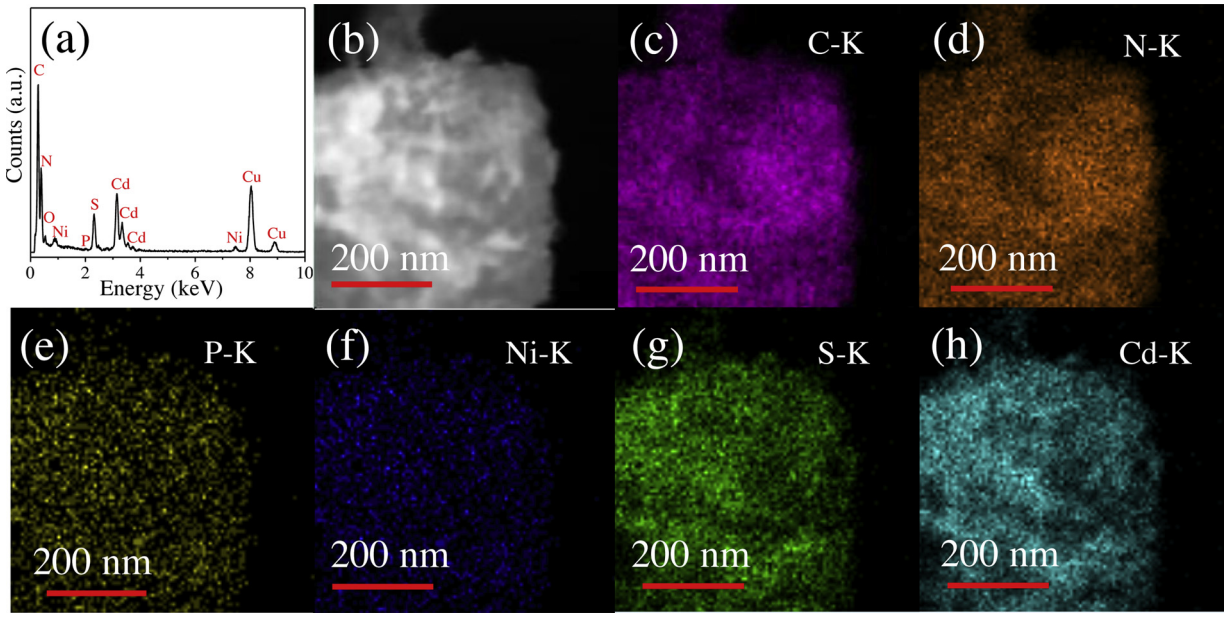

Fig. 6. (a) EDX spectrum, (b) TEM image and (c)-(*j*) STEM-EDX elemental mapping images of $CdS/Ni_2P/g\text{-}C_3N_4$.

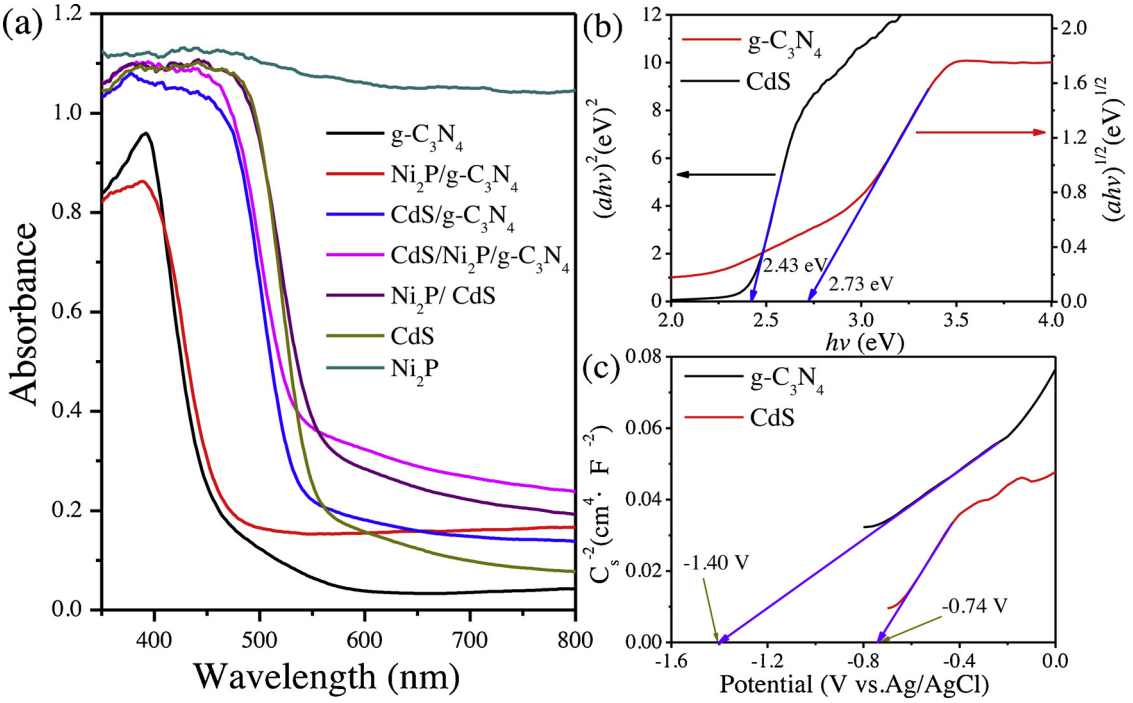

Fig. 7. (a) The UV–vis diffuse reflectance spectra of $CdS/Ni_2P/g\text{-}C_3N_4$ and corresponding reference samples, (b) the band gap energies and (c) Mott-Schottky curves of $g\text{-}C_3N_4$ and CdS.

853.0 eV for Ni 2p element (Fig. 3d), respectively. The peaks located at 853.0 and 869.7 eV are the characteristics of $Ni^{\delta+}$ in Ni_2P [38,51]. The two main peaks at 873.5 and 855.8 eV are assigned to the Ni $2p_{1/2}$ and Ni $2p_{3/2}$ separately, meanwhile two satellite peaks both at 880.5 and 861.8 eV correspond to the surface nickel oxides [52]. The P 2p peaks (Fig. 3e) located at 129.5 and 133.3 eV are attributed to the $P^{\delta-}$ in Ni_2P and surface metal phosphate salts [51,53], respectively. The XPS spectra of Ni 2p and P 2p are not smooth due to the low content of Ni_2P in $CdS/Ni_2P/g\text{-}C_3N_4$ sample [38]. It should be pointed out that the peak intensity for $P^{\delta-}$ of the $CdS/Ni_2P/g\text{-}C_3N_4$ sample is smaller than that of pure Ni_2P, this might be caused by the formation of metal phosphate salts on the surface of Ni_2P during the solvothermal process for the synthesis of CdS [42,53]. Fig. 3f shows that the peaks of Cd element are situated at 412.3 and 405.4 eV, which are attributed to Cd $3d_{5/2}$ and Cd $3d_{3/2}$, respectively, indicating the chemical valence of Cd element is +2 [35]. In addition, the peaks of S element (Fig. 3g) around 162.5 and 161.3 eV belong to the S $2p_{1/2}$ and S $2p_{3/2}$, respectively, suggesting that the state of S element is −2 [54,55]. The above XPS results confirm that ternary $CdS/Ni_2P/g\text{-}C_3N_4$ composite was successfully fabricated.

3.1.3. SEM analysis

The morphology of the as-synthesized samples was studied by SEM. As can be seen, $g\text{-}C_3N_4$ (Fig. 4a) has irregular morphology and is composed of a large quantity of nanosheets with length of 100–400 nm.

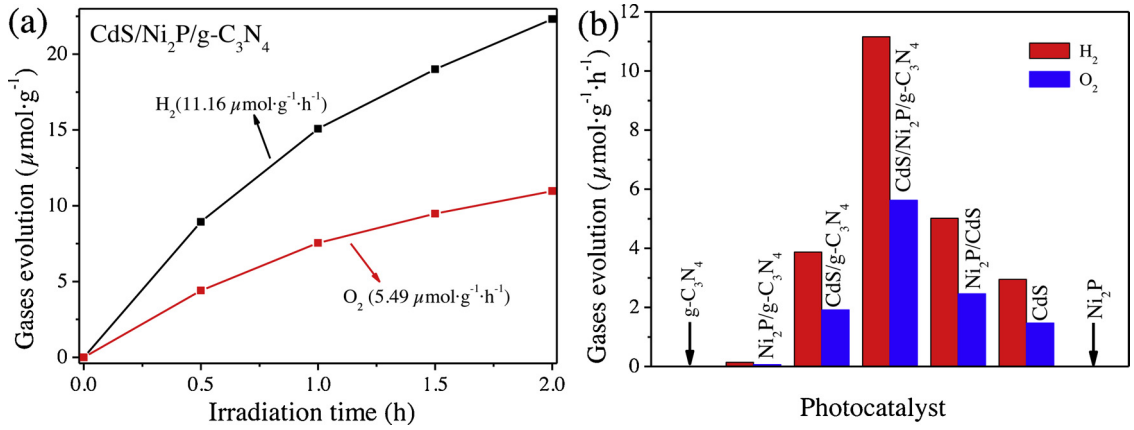

Fig. 8. (a) The photocatalytic activity of CdS/Ni_2P/g-C_3N_4 for evolution of H_2 and O_2 in pure water under visible light (λ > 420 nm) and (b) corresponding evolution rates of H_2 and O_2 over CdS/Ni_2P/g-C_3N_4 and reference samples.

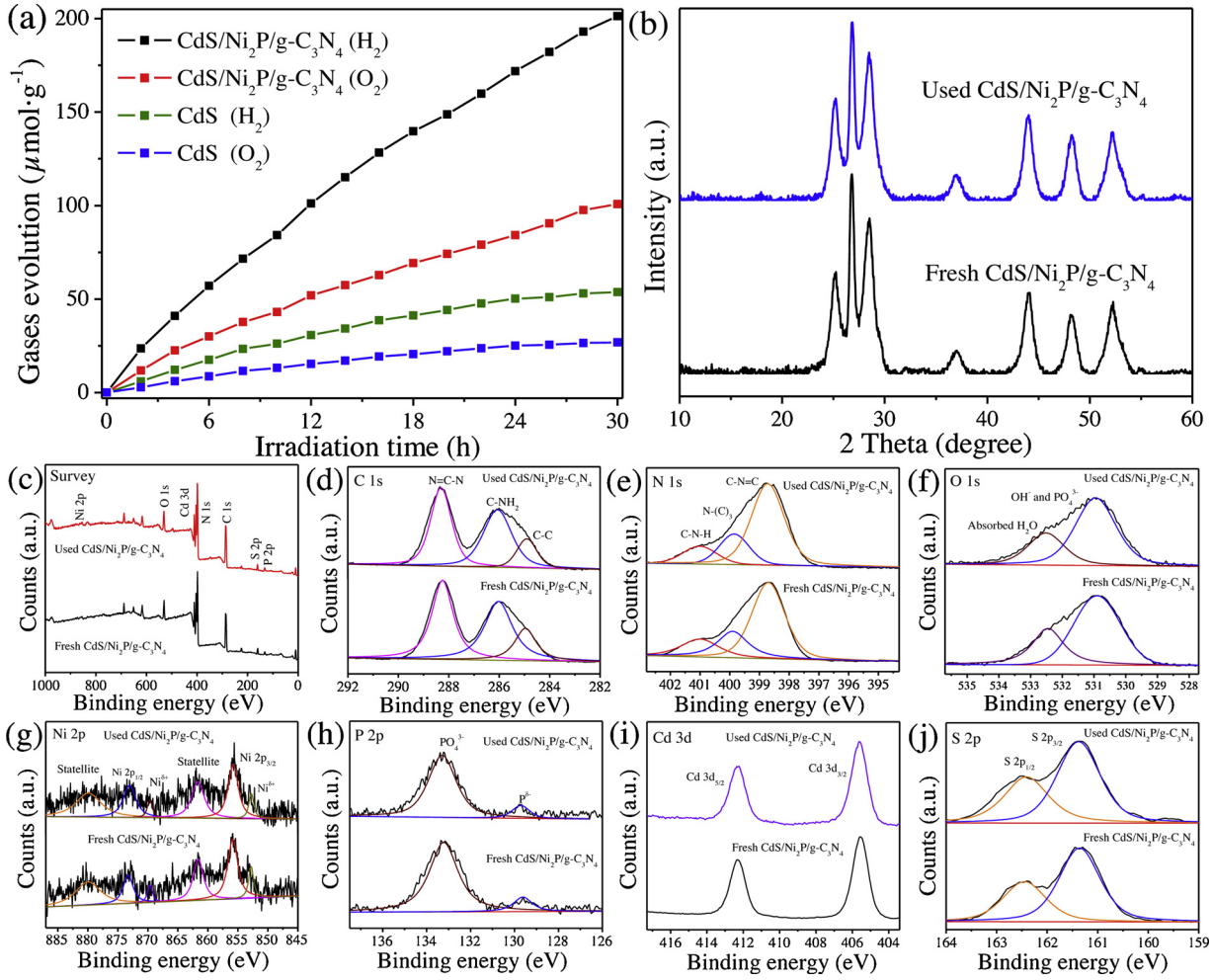

Fig. 9. (a) Photocatalytic evolution of H_2 and O_2 over CdS/Ni_2P/g-C_3N_4 and CdS after prolonged irradiation for 30 h under visible light (λ > 420 nm), (b) XRD patterns of fresh and used CdS/Ni_2P/g-C_3N_4 samples and (c)-(*j*) XPS spectra of fresh and used CdS/Ni_2P/g-C_3N_4 samples.

In Fig. 4b, pure CdS has nanorods structure with length of 50–120 nm. As for the Ni_2P/g-C_3N_4 (Fig. 4c), no Ni_2P nanoparticles can be found obviously on the surface of g-C_3N_4 nanosheets, this is caused by the low content and small particle size of Ni_2P. Differently, some CdS nanorods are coated on the surface of g-C_3N_4 substrate when a certain amount of CdS was loaded for the formation of CdS/g-C_3N_4 composite (Fig. 4d). Similarly, Ni_2P nanoparticles cannot be found obviously on the surface of CdS nanorods for Ni_2P/CdS composite (Fig. 4e). In addition, CdS, Ni_2P and g-C_3N_4 components flock together therefore the CdS/Ni_2P/g-C_3N_4 composite (Fig. 4f) is also of irregular morphology.

The BET specific surface areas of the samples were characterized and calculated to be 25.65, 42.97, 57.10, 10.58, 1.47, 39.20 and 2.94 m^2/g for Ni_2P, g-C_3N_4, CdS, Ni_2P/g-C_3N_4, CdS/g-C_3N_4, Ni_2P/CdS and CdS/Ni_2P/g-C_3N_4, respectively. The decrease in the BET specific surface area of ternary CdS/Ni_2P/g-C_3N_4 catalyst is mainly ascribed to the aggregation of particles caused by continuously hydrothermal and

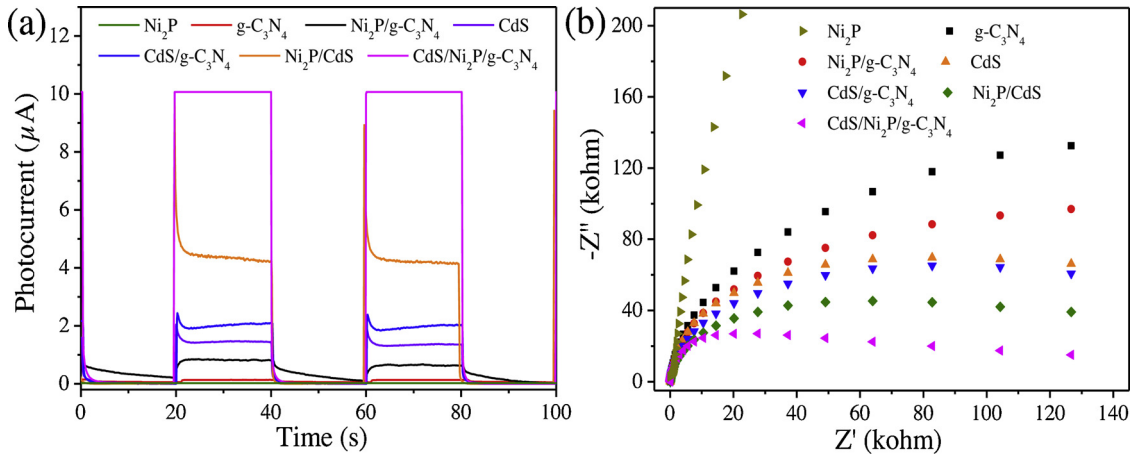

Fig. 10. (a) Transient photocurrent spectra and (b) electrochemical impendence spectra of the as-prepared samples.

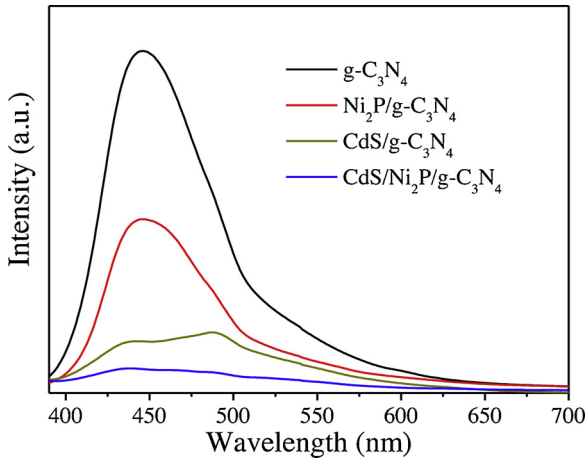

Fig. 11. Photoluminescence spectra of the as-prepared samples.

solvothermal synthetic processes.

3.1.4. HRTEM analysis

The TEM, HRTEM and the STEM-EDX elemental mapping were further explored to capture the subtle structural information of ternary CdS/Ni_2P/g-C_3N_4 composite. As shown in Fig. 5a and b, there exist Ni_2P nanoparticles and CdS nanorods on the g-C_3N_4 nanosheets. The corresponding HRTEM images in Fig. 5c and d give the more detailed structural information of CdS, Ni_2P and g-C_3N_4. Namely, an interplanar spacing of 0.326 nm is in accordance with the (002) plane of g-C_3N_4. Besides, the interplanar spacing of 0.220 nm originates from the (111) lattice plane of Ni_2P [56]. In addition, the lattice spacing of CdS is observed to be 0.316 nm, corresponding to (101) plane of CdS. That is to say, a little amount of CdS and Ni_2P can deposit on the surface of g-C_3N_4 substrate easily. Based on this reaction process, the Ni_2P nanoparticles were stuck in the middle of CdS and g-C_3N_4, in which Ni_2P acted as a physical bridge to connect CdS and g-C_3N_4.

Moreover, the EDX spectrum (Fig. 6a) shows that CdS/Ni_2P/g-C_3N_4 composite consists of C, N, P, Ni, S and Cd elements, except for the Cu and O elements coming from the carbon-coated copper grid substrate and the conducting resin [57]. Simultaneously, the EDX mapping images also indicate the existence of C, N, P, Ni, S and Cd elements. The low signal intensity of Ni and P likewise ensures the low content of Ni_2P component in CdS/Ni_2P/g-C_3N_4 composite (Fig. 6e and 6f).

3.1.5. DRS analysis

The light absorption properties of as-prepared samples were

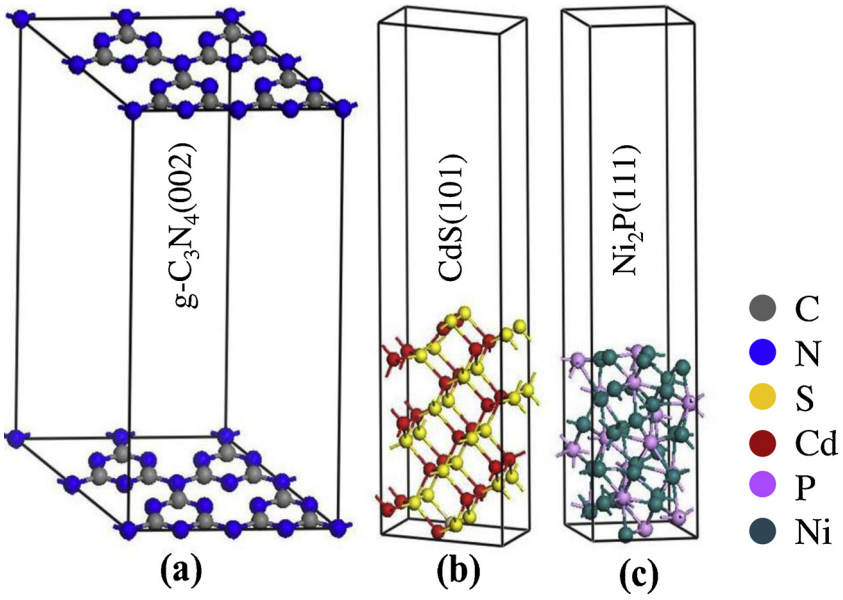

Fig. 12. Optimized structures of (a) g-C_3N_4 (002), (b) CdS (101) and (c) Ni_2P (111) planes.

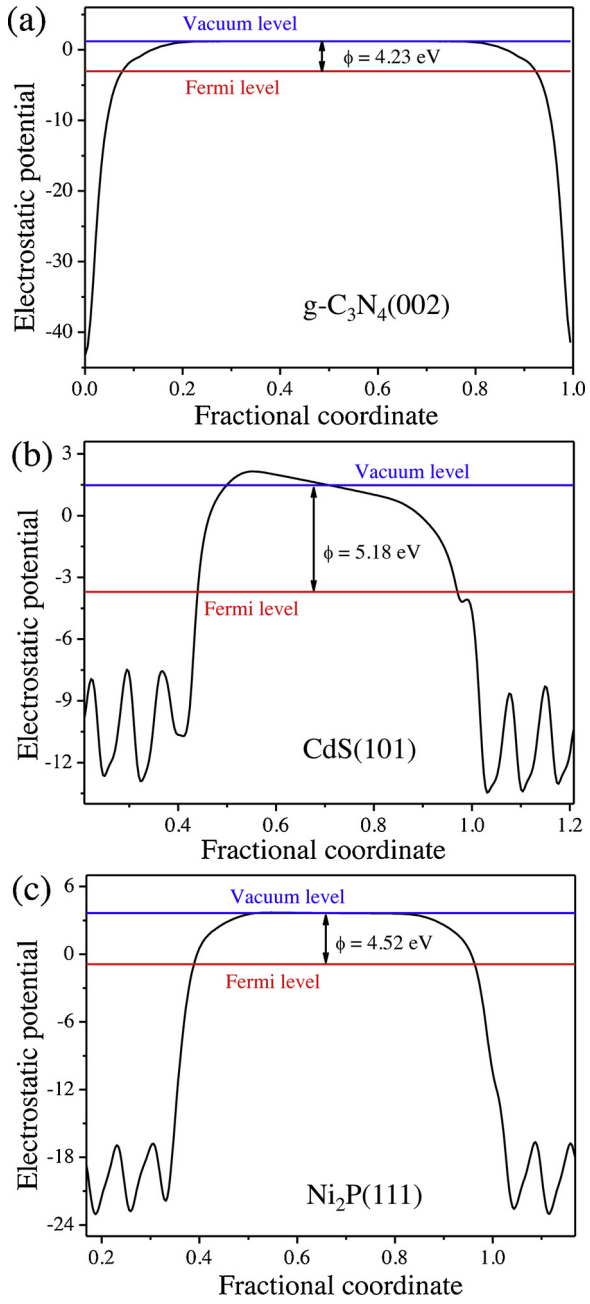

Fig. 13. Calculated Fermi levels of (a) g-C_3N_4 (002), (b) CdS (101) and (c) Ni_2P (111) planes.

measured by UV–vis diffuse reflectance spectra and the result is shown in Fig. 7. Fig. 7a shows that the visible light absorption performance increases following the order: g-C_3N_4 < CdS < Ni_2P. For pure g-C_3N_4 and CdS, the corresponding absorption edges locate at about 453 and 531 nm, respectively. After loading CdS or Ni_2P, the visible light absorption range of g-C_3N_4 broadens obviously. Based on the data in Fig. 7a, the corresponding band gap energies (E_g) of g-C_3N_4 and CdS were estimated by formula (1) [58] and provided in Fig. 7b.

$$\alpha h\nu = A(h\nu - E_g)^{n/2} \quad (1)$$

Where α is the absorption coefficient, h is the Planck's constant, A is a constant, ν is the light frequency, E_g is band gap energy, and the n value is determined by the type of optical transition of semiconductor (n = 1 and 4) with direct or indirect band characteristics. According to the reported literatures, g-C_3N_4 [59] and CdS [60] belong to indirect and direct band semiconductors, respectively. Thus, the E_g values of g-C_3N_4 and CdS are calculated to be about 2.73 and 2.43 eV, respectively.

In order to estimate the conduction band potential (E_{CB}) and valance band potential (E_{VB}) of g-C_3N_4 and CdS, their corresponding Mott-Schottky curves were measured in detail [61]. Fig. 7c shows that both g-C_3N_4 and CdS belong to n-type semiconductors owing to their positive slopes of the C^{-2}-E plots [62]. Via extrapolating the Mott-Schottky curves, the flat band potentials (V_{fb}) equal -1.40 V and -0.74 V vs. Ag/AgCl at pH = 6.8 for g-C_3N_4 and CdS in phosphate buffered saline solution, respectively. In other words, the above V_{fb} values are -1.20 V and -0.54 V vs. NHE at pH = 6.8 [61], respectively. According to literature [63], the E_{CB} value of an n-type semiconductor is very close to its V_{fb} value. So, the E_{CB} values of g-C_3N_4 and CdS approximately equal to be -1.20 V and -0.54 V vs. NHE at pH = 6.8, respectively. Next, the E_{VB} values of g-C_3N_4 and CdS are estimated to be 1.53 V and 1.89 V, respectively, based on the following equation: $E_{CB} = E_{VB}$-E_g. Thus, g-C_3N_4 and CdS have matched type II energy band structure, which facilitates the transfer of photocarriers [11,64,65].

3.2. Photocatalytic activity of CdS/Ni_2P/g-C_3N_4

The photocatalytic activity of CdS/Ni_2P/g-C_3N_4 was evaluated by overall water splitting into H_2 and O_2 under visible light (λ > 420 nm). As shown in Fig. 8a, the evolution amount of H_2 and O_2 over CdS/Ni_2P/g-C_3N_4 are 22.32 and 11.24 μmol g^{-1} after 2 h irradiation, respectively, which meets the stoichiometric ratio of 2:1 approximately. This result indicates that the novel ternary CdS/Ni_2P/g-C_3N_4 system can split water completely.

As comparison, the photocatalytic performances of the reference samples were further explored. Fig. 8b presents that, pure Ni_2P and g-C_3N_4 cannot yield measurable H_2 and O_2 under visible light, due to the rapid photocarriers recombination rate. The other samples including Ni_2P/g-C_3N_4, CdS/g-C_3N_4, CdS/Ni_2P/g-C_3N_4, Ni_2P/CdS and CdS display different H_2/O_2 evolution rates as 0.14/0.062, 3.87/1.91, 11.16/5.62, 5.02/2.46 and 2.95/1.47 μmol g^{-1} h^{-1}, respectively. As is well-known, overall water splitting achieved by semiconductor photocatalyst fully reflects the intrinsic separation efficiency of photocarriers on condition that they have suitable energy band structure for H_2/O_2 evolution. Among the above-mentioned various photocatalysts, ternary CdS/Ni_2P/g-C_3N_4 exhibits the best overall water splitting activity, which suggests that CdS/Ni_2P/g-C_3N_4 has strong separation efficiency of photocarriers.

In addition, we further explored the effect of Ni_2P content (0.5–10 wt%) on the activity of CdS/Ni_2P/g-C_3N_4 (Fig. S1). It can be found that, the H_2/O_2 evolution rates of CdS/0.5%Ni_2P/g-C_3N_4, CdS/1.3%Ni_2P/g-C_3N_4, CdS/3%Ni_2P/g-C_3N_4, CdS/5%Ni_2P/g-C_3N_4 and CdS/10%Ni_2P/g-C_3N_4 are 6.26/3.05, 11.16/5.62, 15.56/7.75, 12.68/6.32 and 8.56/4.26 μmol g^{-1} h^{-1}. The photocatalytic activity of CdS/Ni_2P/g-C_3N_4 composites decreases when Ni_2P content exceeds 3 wt%. Therefore, appropriate Ni_2P content has the maximal transfer ability for the separation of interface electrons of CdS/g-C_3N_4. Furthermore, the apparent quantum efficiency (AQE) value of CdS/1.3%Ni_2P/g-C_3N_4 photocatalyst was measured to be 0.18% under the irradiation of 420 nm monochromatic light [35].

3.3. Stability of CdS/Ni_2P/g-C_3N_4

In order to investigate the stability of photocatalyst in photocatalytic process, ternary CdS/Ni_2P/g-C_3N_4 and pure CdS reference sample were successively irradiated for 30 h under visible light (λ > 420 nm). Fig. 9a displays that the amounts of H_2 and O_2 generated by CdS/Ni_2P/g-C_3N_4 progressively increase and reach to 201.32 and 100.81 μmol g^{-1} after 30 h irradiation, respectively. This confirms that CdS/Ni_2P/g-C_3N_4 still keeps outstanding H_2/O_2 evolution activity after a long period of irradiation time. As a reference, the amounts of H_2 and O_2 produced by pure CdS do not increase obviously after 24 h irradiation, thus merely reach to 53.76 and 26.9 μmol g^{-1} after 30 h

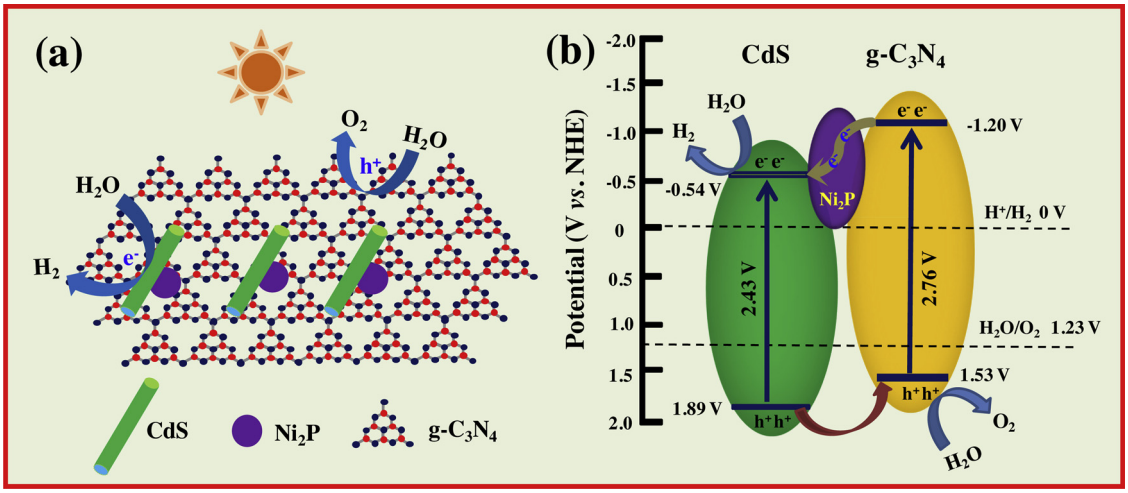

Fig. 14. Photocarriers separation mechanism of ternary CdS/Ni_2P/g-C_3N_4 under visible light (λ > 420 nm).

irradiation due to the inevitable photocorrosion of CdS [66]. The XRD patterns (Fig. 9b) and XPS spectra (Fig. 9c-j) of the fresh and used CdS/Ni_2P/g-C_3N_4 samples indicate that the crystalline structure and chemical states of the sample do not change obviously in the photocatalytic process. That is to say, the CdS/Ni_2P/g-C_3N_4 is of high activity and high stability for overall water splitting. It is particularly pointed out that, the O 1 s XPS spectrum (Fig. 9f) includes two peaks located at 532.5 and 530.9 eV, one peak located at 530.9 eV corresponds to OH^- and PO_4^{3-} [40,41]. The existence of PO_4^{3-} may be the byproduct of excess red P and H_2O interaction in hydrothermal process [42,53]. The other peak located at 532.5 eV is related with adsorbed H_2O molecules [41].

3.4. Photocarriers separation

In general, the activity of photocatalyst mainly depends on the separation of photocarriers, which pushes us to investigate the reason of excellent activity of CdS/Ni_2P/g-C_3N_4 composite. Here, transient photocurrent (TPC) spectra, electrochemical impendence spectroscopy (EIS) and photoluminescence (PL) spectra are measured to reflect the law of photocarriers separation in the photocatalytic process.

Because the TPC intensity has positive correlation to the separation of photocarriers, it is widely used to explain the activity changes of the photocatalysts [67]. As shown in Fig. 10a, all the samples display TPC response signals under visible light (λ > 420 nm) except for Ni_2P, among which CdS/Ni_2P/g-C_3N_4 composite possesses the highest TPC intensity, indicating that CdS/Ni_2P/g-C_3N_4 has the best separation efficiency of photocarriers under the same condition. It can also be seen that, the change in the TPC intensity and photocatalytic activity of samples has perfect correspondence, ensuring the outstanding activity of CdS/Ni_2P/g-C_3N_4 results from the superior separation efficiency of photocarriers.

EIS was further measured to help us comprehend the separation resistance of photocarriers in the migration process. The smallest arc radius for ternary CdS/Ni_2P/g-C_3N_4 sample (Fig. 10b) proves the minimum separation resistance of photocarriers in comparison with the pure and binary samples [68]. That is, CdS/Ni_2P/g-C_3N_4 possesses the best separation efficiency of photocarriers in all the samples.

Except for the above-mentioned electrochemical analysis, mutual authentication is necessary by using PL spectra, due to its extensive use for understanding the charge transfer, recombination and photoelectron lifetime [69]. Under irradiation of 370 nm light, pure g-C_3N_4 exhibits a high PL emission peak at 445 nm (Fig. 11). The binary Ni_2P/g-C_3N_4 and CdS/g-C_3N_4 obviously decrease the PL intensity compared to g-C_3N_4, indicating the positive role of Ni_2P or CdS on the photocarriers. More importantly, CdS/Ni_2P/g-C_3N_4 presents the lowest PL intensity among the samples. This testifies the highest separation efficiency of photocarriers for CdS/Ni_2P/g-C_3N_4 composite once again.

3.5. Structure and computational detail

The work function is one of important parameters in estimating the charge transfer direction between the interfaces of semiconductor materials. So, the work functions of g-C_3N_4 (002), CdS (101) and Ni_2P (111) planes were calculated according to the HRTEM results (Fig. 5). First principle density functional theory (DFT) calculations were carried out by CASTEP module of Materials Studio software. The Perdew-Burke-Ernzerhof (PBE) form exchange-correlation functional was adopted within the generalized gradient approximation (GGA). A cutoff energy of 450 eV and a Monkhorst Pack k-mesh of 3 × 3 × 1 for g-C_3N_4, 2 × 3 × 1 for CdS and 4 × 4 × 1 for Ni_2P were employed. The convergence criteria of geometry optimization were set as 5.0×10^{-6} eV per atom for energy, 0.01 eV per Å for maximum force, 0.02 GPa for maximum pressure and 5.0×10^{-4} Å for maximum displacement. The optimized structures of g-C_3N_4 (002), CdS (101) and Ni_2P (111) planes are listed in Fig. 12. After geometry optimization, the average potential profile of g-C_3N_4 (002), CdS (101) and Ni_2P (111) planes were calculated to obtain their work functions. The work function (Φ) can be defined as $\Phi = E_{vac}\text{-}E_F$, here E_{vac} and E_F are the vacuum energy and Fermi energy of semiconductor, respectively.

As a result, the calculated work functions of the g-C_3N_4 (002), CdS (101) and Ni_2P (111) planes are 4.23, 5.18 and 4.52 eV, respectively (Fig. 13). From their work functions, we can find that the Fermi energy of the g-C_3N_4 (002) surfaces is higher than those of CdS (101) and Ni_2P (111) surface, and the Fermi energy of the CdS (101) surface is lower than those of g-C_3N_4 (002) and Ni_2P (111) surfaces. During the photocatalytic process, electrons will transfer from one semiconductor with a higher Fermi level to the other one with a lower Fermi level. Therefore, electrons will transfer from g-C_3N_4 to Ni_2P and CdS or transfer from Ni_2P to CdS in the hybridization process, implying the formation of built-in electric field among g-C_3N_4, Ni_2P and CdS interfaces, and the direction of built-in electric field is from g-C_3N_4 to Ni_2P or from Ni_2P to CdS, which is beneficial to the separation and diffusion of photogenerated charge carriers.

Based on the above analysis, a proposed mechanism for photocatalytic H_2 and O_2 evolution over CdS/Ni_2P/g-C_3N_4 sample is illustrated in Fig. 14. The CdS/Ni_2P/g-C_3N_4 composite with special structure was constructed, in which Ni_2P nanoparticles acting as a physical bridge were stuck in the middle of CdS and g-C_3N_4 (Fig. 14a). Under visible light (λ > 420 nm), the photoinduced electrons on the conduction band of g-C_3N_4 transfer to Ni_2P quickly, and then further move

to the conduction band of CdS. During the photocarriers separation process, Ni_2P serves as an excellent electron-bridge from g-C_3N_4 to CdS and reduces the transfer resistance of electrons remarkably due to its good electrical conductivity. As a result, the photoinduced electrons accumulated on the conduction band (− 0.54 V) of CdS will reduce H_2O to H_2 efficiently, meanwhile the photoinduced holes assembled on the valence band (1.89 V) of g-C_3N_4 will oxidize H_2O to O_2. In this process, Ni_2P is mainly regarded as a novel electron-bridge to reduce the transfer resistance of photoinduced electrons as well as to endow superior overall water splitting activity of CdS/Ni_2P/g-C_3N_4 than the binary Ni_2P/g-C_3N_4, Ni_2P/CdS and CdS/g-C_3N_4 samples.

4. Conclusions

In this study, we successfully designed a distinctive ternary CdS/Ni_2P/g-C_3N_4 composite to achieve highly efficient overall water splitting performance. The as-prepared CdS/Ni_2P/g-C_3N_4 composite with 3 wt% Ni_2P exhibited the highest H_2 and O_2 evolution rates with 15.56 and 7.75 $\mu mol \cdot g^{-1} h^{-1}$, respectively, which is 3.10 and 4.02 times higher than those of binary Ni_2P/CdS and CdS/g-C_3N_4. The outstanding activity of CdS/Ni_2P/g-C_3N_4 lies in the important interface electron transfer role of Ni_2P as electron-bridge in CdS/g-C_3N_4 heterojuction. Furthermore, the ternary CdS/Ni_2P/g-C_3N_4 composite also displayed good stability for H_2 and O_2 evolution. This work provides a guideline for the rational design of highly efficient TMPs-based ternary composite for overall water splitting under visible light.

Acknowledgements

This work was financially supported by the Natural Science Foundation of China (51772118, 51472005), the Anhui Provincial Natural Science Foundation (1708085MB32), State Key Laboratory of Structural Chemistry (20160014) and Anhui Provincial Innovation Team of Design and Application of Advanced Energetic Materials (KJ2015TD003).

Appendix A. Supplementary data

Supplementary material related to this article can be found, in the online version, at doi:https://doi.org/10.1016/j.apcatb.2019.02.055.

References

[1] K. Maeda, T. Takata, M. Hara, N. Saito, Y. Inoue, H. Kobayashi, K. Domen, J. Am. Chem. Soc. 127 (2005) 8286–8287.
[2] M. Higashi, R. Abe, T. Takata, K. Domen, Chem. Mater. 21 (2009) 1543–1549.
[3] R. Abe, T. Takata, H. Sugihara, K. Domen, Chem. Commun. 30 (2005) 3829–3831.
[4] K. Maeda, K. Domen, J. Phys. Chem. Lett. 1 (2010) 2655–2661.
[5] L. Jiao, Y.X. Zhou, H.L. Jiang, Chem. Sci. 7 (2016) 1690–1695.
[6] Y.Y. WU, G.D. Li, Y.P. Liu, L. Yang, X.R. Lian, T. Asefa, X.R. Zou, Adv. Funct. Mater. 26 (2016) 4839–4847.
[7] C. Zhu, C.G. Liu, Y.J. Zhou, Y.J. Fu, S.J. Guo, H. Li, S.Q. Zhao, H. Huang, Y. Liu, Z.H. Kang, Appl. Catal. B Environ. 216 (2017) 114–121.
[8] G.G. Zhang, Z.A. Lan, L.H. Lin, S. Lin, X.C. Wang, Chem. Sci. 7 (2016) 3062–3066.
[9] Z. Liu, P.F. Fang, S.J. Wang, Y.P. Gao, F.T. Chen, F. Zheng, Y. Liu, Y.Q. Dai, J. Mol. Catal. A Chem. 363 (2012) 159–165.
[10] F. Dong, Z.W. Zhao, T. Xiong, Z.L. Ni, W.D. Zhang, Y.J. Sun, W.K. Ho, ACS Appl. Mater. Int. 5 (2013) 11392–11401.
[11] X. Dai, M.L. Xie, S.G. Meng, X.L. Fu, S.F. Chen, Appl. Catal. B Environ. 158–159 (2014) 382–390.
[12] J.Y. Zhang, Y.H. Wang, J. Jin, J. Zhang, Z. Lin, F. Huang, J.G. Yu, ACS Appl. Mater. Int. 5 (2013) 10317–10324.
[13] Y.J. Zou, J.W. Shi, D.D. Ma, Z.Y. Fan, C.M. Niu, L.Z. Wang, ChemCatChem 9 (2017) 3752–3761.
[14] M.Z. You, J.Q. Pan, C.Y. Chi, B.B. Wang, W.J. Zhao, C.S. Song, Y.Y. Zheng, C.R. Li, J. Mater. Sci. 53 (2017) 1978–1986.
[15] T.T. Isimjan, P. Maity, J. Llorca, T. Ahmed, M.R. Parida, O.F. Mohammed, H. Idriss, ACS Omega 2 (2017) 4828–4837.
[16] Z.L. Li, J.C. Lyu, K.L. Sun, M. Ge, Mater. Lett. 214 (2018) 257–260.
[17] H.G. Kim, E.D. Jeong, P.H. Borse, S. Jeon, K. Yong, J.S. Lee, W. Li, S.H. Oh, Appl. Phys. Lett. 89 (2006) 064103.
[18] Z. Zhao, Y.B. Xing, H.B. Li, P.Y. Feng, Z.C. Sun, Sci. China Mater. 61 (2018) 851–860.
[19] W.K. Jo, N.C.S. Selvam, Chem. Eng. J. 317 (2017) 913–924.
[20] A. Iwase, Y.H. Ng, Y. Ishiguro, A. Kudo, R. Amal, J. Am. Chem. Soc. 133 (2011) 11054–11057.
[21] P. Li, Y. Zhou, H.J. Li, Q.F. Xu, X.G. Meng, X.Y. Wang, M. Xiao, Z.G. Zou, Chem. Commun. 51 (2015) 800–803.
[22] J.B. Pan, J.J. Liu, S.L. Zuo, U.A. Khan, Y.C. Yu, B.S. Li, Appl. Surf. Sci. 444 (2018) 177–186.
[23] X.Q. Wu, J. Zhao, L.P. Wang, M.M. Han, M.L. Zhang, H.B. Wang, H. Wang, Y. Liu, Z.H. Kang, Appl. Catal. B Environ. 206 (2017) 501–509.
[24] J. Wang, Y. Xia, H.H. Zhao, G.F. Wang, L. Xiang, J.L. Xu, S. Komarneni, Appl. Catal. B Environ. 206 (2017) 406–416.
[25] S. Sultana, S. Mansingh, K.M. Parida, J. Phys. Chem. C 122 (2017) 808–819.
[26] S.X. Lu, H.H. Xu, B.Y. Gao, L.L. Ren, New J. Chem. 41 (2017) 8497–8502.
[27] R. Prins, M.E. Bussell, Catal. Lett. 142 (2012) 1413–1436.
[28] H. Song, J. Wang, Z.D. Wang, H.L. Song, F. Li, Z.S. Jin, J. Catal. 311 (2014) 257–265.
[29] A.M. Alexander, J.S.J. Hargreaves, Chem. Soc. Rev. 39 (2010) 4388–4401.
[30] E.J. Popczun, J.R. Mckone, C.G. Read, A.J. Biacchi, A.M. Wiltrout, N.S. Lewis, R.E. Schaak, J. Am. Chem. Soc. 135 (2013) 9267–9270.
[31] Z.J. Sun, H.F. Zheng, J.S. Li, P.W. Du, Energy Environ. Sci. 8 (2015) 2668–2676.
[32] Y. Li, M.A. Malik, P. O'Brien, J. Am. Chem. Soc. 127 (2005) 16020–16021.
[33] P. Niu, L.L. Zhang, G. Liu, H.M. Cheng, Adv. Funct. Mater. 22 (2012) 4763–4770.
[34] Y.Y. Deng, Y. Zhou, Y. Yao, J. Wang, New J. Chem. 37 (2013) 4083–4088.
[35] M.Y. Zhang, H.L. Lin, J. Cao, X.M. Guo, S.F. Chen, Chem. Eng. J. 321 (2017) 484–494.
[36] L. Ge, C.C. Han, J. Liu, Y.F. Li, Appl. Catal. A Gen. 409–410 (2011) 215–222.
[37] H. Zhao, S.G. Sun, P.P. Jiang, Z.J. Xu, Chem. Eng. J. 315 (2017) 296–303.
[38] W.J. Wang, T.C. An, G.Y. Li, D.H. Xia, H.J. Zhao, C.Y. Jimmy, P.K. Wong, Appl. Catal. B Environ. 217 (2017) 570–580.
[39] Y. Xu, W.D. Zhang, Eur. J. Inorg. Chem. 2015 (2015) 1744–1751.
[40] J.J. Li, M.C. Liu, L.B. Kong, D. Wang, Y.M. Hu, W. Han, L. Kang, RSC Adv. 5 (2015) 41721–41728.
[41] J. Wang, J.Y. Yang, Z.Y. Zheng, T.B. Lu, W.H. Gao, Appl. Catal. B Environ. 218 (2017) 277–286.
[42] B. Wang, X. Huang, Z.B. Zhu, H. Huang, J.H. Dai, Int. J. Mater. Res. 104 (2013) 507–510.
[43] L.Q. Ye, C.Q. Han, Z.Y. Ma, Y.M. Leng, J. Li, X.X. Ji, D.Q. Bi, H.Q. Xie, Z.X. Huang, Chem. Eng. J. 307 (2017) 311–318.
[44] X.L. Yin, L.L. Li, W.J. Jiang, Y. Zhang, X. Zhang, L.J. Wan, J.S. Hu, ACS Appl. Mater. Inter. 8 (2016) 15258–15266.
[45] S.S. Yi, J.M. Yan, B.R. Wulan, S.J. Li, K.H. Liu, Q. Jiang, Appl. Catal. B Environ. 200 (2017) 477–483.
[46] Q.H. Liang, Z. Li, X.L. Yu, Z.H. Huang, F.Y. Kang, Q.H. Yang, Adv. Mater. 27 (2015) 4634–4639.
[47] J.S. Zhang, M.W. Zhang, G.G. Zhang, X.C. Wang, ACS Catal. 2 (2012) 940–948.
[48] Y. Xu, Z.C. Fu, S. Cao, Y. Chen, W.F. Fu, Catal. Sci. Technol. 7 (2017) 587–595.
[49] J. Jiang, J.G. Yu, S.W. Cao, J. Colloid Interface Sci. 461 (2016) 53–56.
[50] Q.Y. Lin, L. Li, S.J. Liang, M.H. Liu, J.H. Bi, L. Wu, Appl. Catal. B Environ. 163 (2015) 135–142.
[51] T.T. Sun, J. Dong, Y. Huang, W. Ran, J.F. Chen, L.B. Xu, J. Mater. Chem. A 6 (2018) 12751–12758.
[52] S.H. Li, N. Zhang, X.Q. Xie, R. Luque, Y.J. Xu, Angew. Chem. Int. Ed. 130 (2018) 13266–13269.
[53] D. Zhang, G.L. Li, J.Y. Xiang, Mater. Res. Bull. 85 (2017) 147–151.
[54] X.Z. Zhou, J.J. Huang, H.Z. Zhang, H. Sun, W.X. Tu, Int. J. Hydrogen Energy 33 (2016) 14758–14767.
[55] X. Zong, J.F. Han, G.J. Ma, H.J. Yan, G.P. Wu, C. Li, J. Phys. Chem. C 115 (2011) 12202–12208.
[56] S. Cao, Y. Chen, C.J. Wang, P. He, W.F. Fu, Chem. Commun. 50 (2014) 10427–10429.
[57] S. Cho, J.W. Jang, Y.B. Park, J.Y. Kim, G. Magesh, J.H. Kim, M. Seol, K. Yong, K.H. Lee, J.S. Lee, Energy Environ. Sci. 7 (2014) 2301–2307.
[58] X.M. Jia, J. Cao, H.L. Lin, M.Y. Zhang, X.M. Guo, S.F. Chen, Appl. Catal. B Environ. 204 (2017) 505–514.
[59] Y.Z. Hong, Y.H. Jiang, C.S. Li, W.Q. Fan, X. Yan, M. Yan, W.D. Shi, Appl. Catal. B Environ. 180 (2016) 663–673.
[60] X. Jia, M. Tahir, L. Pan, Z.F. Huang, X.W. Zhang, L. Wang, J.J. Zou, Appl. Catal. B Environ. 198 (2016) 154–161.
[61] Y.Y. Bu, Z.Y. Chen, W.B. Li, Appl. Catal. B Environ. 144 (2014) 622–630.
[62] R.P. Hu, X. Xiao, S.H. Tu, X.X. Zuo, J.M. Nan, Appl. Catal. B Environ. 163 (2015) 510–519.
[63] S.X. Weng, B.B. Chen, L.Y. Xie, Z.Y. Zheng, P. Liu, J. Mater. Chem. A 1 (2013) 3068–3075.
[64] Y. Xu, Y. Chen, W.F. Fu, Appl. Catal. B Environ. 236 (2018) 176–183.
[65] J.Y. Zhang, Y.H. Wang, J. Jin, J. Zhang, Z. Lin, F. Huang, J.G. Yu, ACS Appl. Mater. Interface 20 (2013) 10317–10324.
[66] J.L. Yuan, J.Q. Wen, Y.M. Zhong, X. Li, Y.P. Fang, S.S. Zhang, W. Liu, J. Mater. Chem. A 3 (2015) 18244–18255.
[67] M. Kong, Y.Z. Li, X. Chen, T.T. Tian, P.F. Fang, F. Zheng, X.J. Zhao, J. Am. Chem. Soc. 133 (2011) 16414–16417.
[68] C. Han, Z. Chen, N. Zhang, J.C. Colmenares, Y.J. Xu, Adv. Funct. Mater. 25 (2015) 221–229.
[69] X.K. Zeng, Z.Y. Wang, G. Wang, T.R. Gengenbach, D.T. Mccarthy, A. Deletic, J.G. Yu, X.W. Zhang, Appl. Catal. B Environ. 218 (2017) 163–173.